

Direct Visualization of Homogeneous Chemical Distribution in Functional Polyradical Microspheres

Jochen A. Kammerer, Florian Feist, Daniel Ryklin, Abhishek Sarkar, Christopher Barner-Kowollik,* and Rasmus R. Schröder*

It is demonstrated that the postfunctionalization of solid polymeric microspheres can generate fully and throughout functionalized materials, contrary to the expectation that core–shell structures are generated. The full functionalization is illustrated on the example of photochemically generated microspheres, which are subsequently transformed into polyradical systems. Given the all-organic nature of the functionalized microspheres, characterization methods with high analytical sensitivity and spatial resolution are pioneered by directly visualizing the inner chemical distribution of the postfunctionalized microspheres based on characteristic electron energy loss signals in transmission electron microscopy (TEM). Specifically, ultrasonic ultramicrotomy is combined successfully with electron energy loss spectroscopy (EELS) and electron spectroscopic imaging (ESI) during TEM. These findings open a key avenue for analyzing all-organic low-contrast soft-matter material structures, while the specifically investigated system concomitantly holds promise as an all-radical solid-state functional material.

gene delivery,^[4] analytical systems (such as stationary phases for chromatography) to emerging applications in solar cells.^[5] Microspheres have been generated by a wide range of techniques, mostly thermally driven and requiring additives during the synthesis process. Our group has pioneered access methods to microspheres driven by light,^[6–8] and most recently introduced a method that can produce microspheres entirely driven by sunlight, from simple monomers without any additives (refer to **Figure 1**).^[9] Interestingly, these (solid) microspheres can be further modified in their molecular structure by an elimination and subsequent oxidation, generating an extended conjugated system featuring delocalized electrons and a stable neutral radical. Such microspheres should—in principle—be paramagnetic and possibly conducting, critically expanding the scope of application. Herein, we answer the key question if chemical modification to solid microspheres translates through their entire bulk properties or—alternatively—generates core–shell structures, which is the currently assumed structure of microspheres that have

conducting, critically expanding the scope of application. Herein, we answer the key question if chemical modification to solid microspheres translates through their entire bulk properties or—alternatively—generates core–shell structures, which is the currently assumed structure of microspheres that have

1. Introduction

Microspheres—or microparticles—are integral to a wide range of applications, ranging from point-of-care diagnostics (such as home pregnancy^[1] or coronavirus tests^[2]), antigen^[3] and

J. A. Kammerer, D. Ryklin, R. R. Schröder
3DMM2O
Cluster of Excellence (EXC-2082/1–390761711) and Cryo
Electron Microscopy
BioQuant
Heidelberg University and University Hospital
Im Neuenheimer Feld 267, 69120 Heidelberg, Germany
E-mail: rasmus.schroeder@bioquant.uni-heidelberg.de

J. A. Kammerer, C. Barner-Kowollik
School of Chemistry and Physics
Centre for Materials Science
Queensland University of Technology (QUT)
2 George Street, Brisbane QLD 4000, Australia
E-mail: christopher.barnerkowollik@qut.edu.au

F. Feist, C. Barner-Kowollik
3DMM2O
Cluster of Excellence (EXC-2082/1–390761711) and Institute
of Nanotechnology
Karlsruhe Institute of Technology (KIT)
Hermann-von-Helmholtz-Platz 1
76344 Eggenstein-Leopoldshafen, Germany

A. Sarkar
Institute of Nanotechnology (INT)
Karlsruhe Institute of Technology (KIT)
Hermann-von-Helmholtz-Platz 1
76344 Eggenstein-Leopoldshafen, Germany
A. Sarkar
KIT-TUD Joint Research Laboratory Nanomaterials–Technische
Universität Darmstadt
Otto-Berndt-Str. 3, 64287 Darmstadt, Germany

 The ORCID identification number(s) for the author(s) of this article can be found under <https://doi.org/10.1002/adma.202211074>.

© 2023 The Authors. Advanced Materials published by Wiley-VCH GmbH. This is an open access article under the terms of the Creative Commons Attribution-NonCommercial License, which permits use, distribution and reproduction in any medium, provided the original work is properly cited and is not used for commercial purposes.

DOI: 10.1002/adma.202211074

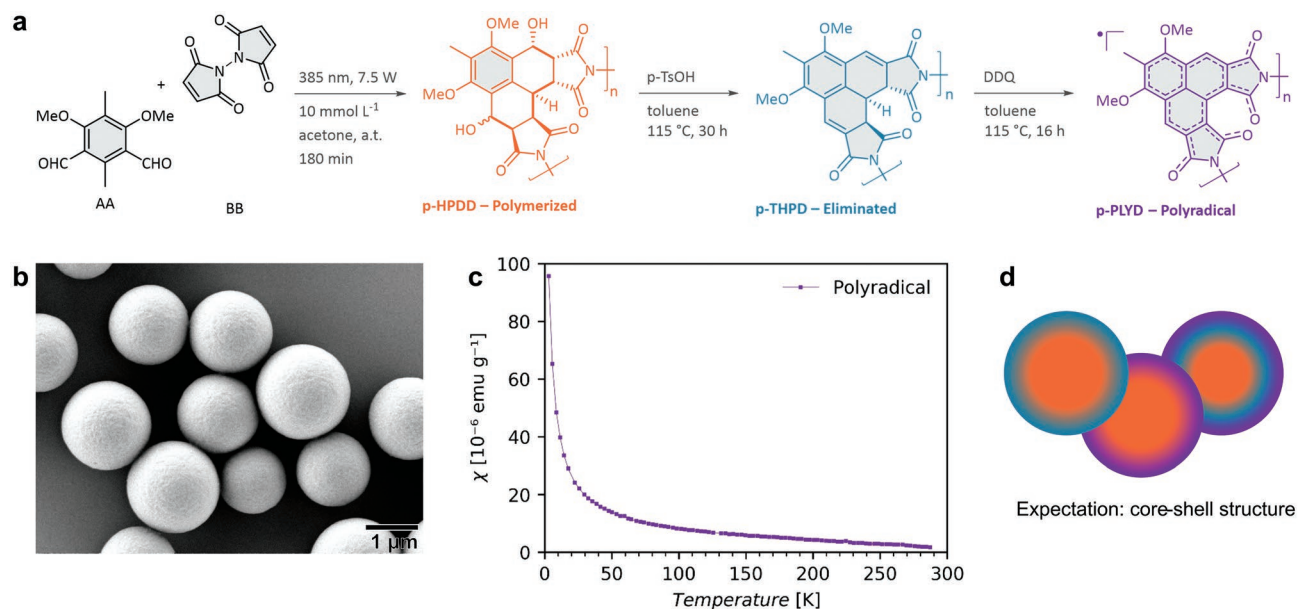


Figure 1. Synthesis and properties of postfunctionalized paramagnetic microspheres with a stable neutral, delocalized polyradical in the backbone. a) Synthesis route to stable neutral polyradical microspheres via a Diels–Alder photopolymerization at ambient temperature (a.t.) and solid-state postfunctionalization by elimination and oxidation. The gray areas indicate delocalized electronic systems. b) Scanning electron microscopy image of the initial microspheres. c) SQUID measurement confirms the polyradical and the paramagnetism of the microspheres. d) The insolubility of the microspheres suggests a diffusion limitation for the elimination and oxidation during the solid-state postfunctionalization. A core–shell-type chemical distribution—as expected—would be detrimental for the applicability of the polyradical due to the limited functionalization.

undergone postfunctionalization.^[4,10] To the best of our knowledge, past analyses of postmodified microspheres focused on changes in their surface chemistry, evidenced by techniques such as X-ray photoelectron spectroscopy (XPS) and time-of-flight secondary-ion mass spectrometry (ToF-SIMS).^[7,11–16] Answering the question how postmodification affects the inner chemical distribution of microspheres is a far more challenging task, which we address herein.

We access the inner chemical spatial distribution of the microsphere with high resolution in the nanometer range by

combining ultrasonic ultramicrotomy with electron energy loss spectroscopy (EELS) and electron spectroscopic imaging (ESI) during transmission electron microscopy (TEM) (Figure 2). By utilizing characteristic electron energy loss signals corresponding to specific optical excitations of the different functionalized materials, we overcome the challenge of insubstantial contrast differences in conventional images of materials with high chemical similarity—here, the initial polymer and its eliminated and polyradical derivatives. We reveal homogeneous highly functionalized polyradical microspheres,

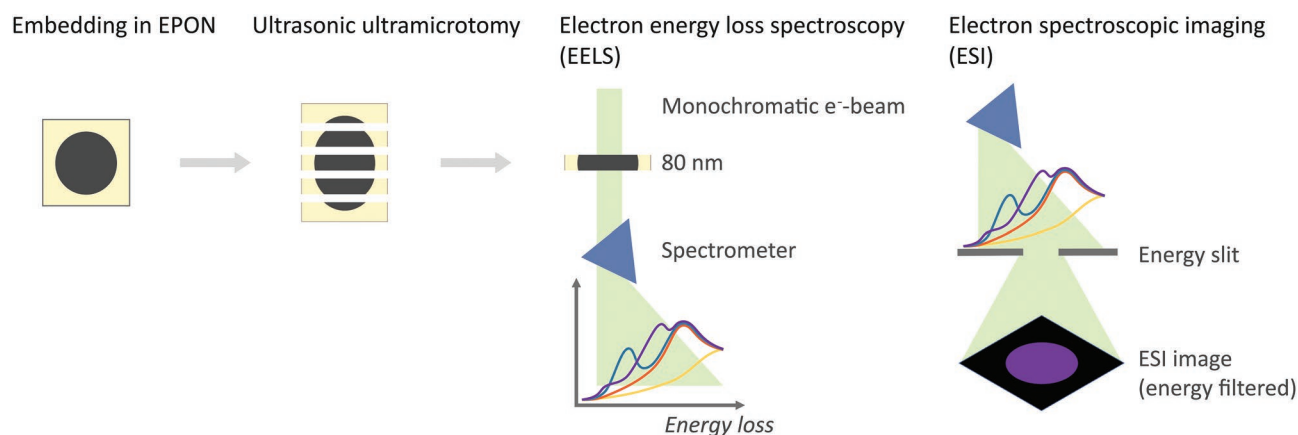


Figure 2. Sample preparation and experimental strategies of EELS and ESI. Sample preparation: The microspheres are embedded in an epoxide resin (EPON) and cut with ultrasonic ultramicrotomy to generate electron transparent sections for TEM with a nominal thickness of 80 nm. EELS: The transmitted inelastically interacting beam electrons lose energy by exciting electronic transitions in the sample. A spectrometer separates the beam electrons according to their energy loss into an EEL spectrum. ESI: Beam electrons of a certain energy loss are selected by an energy slit of 0.8 eV width to form the ESI image.

opposing an expected shell-only functionalization in the solid state. The throughout functionalization of the microspheres is vital proof for the applicability of the described chemical modification scheme to form complex polyradical structures, devices, and metamaterials, as even relatively large micrometer-sized structures can be functionalized efficiently throughout.

2. Results

2.1. Synthesis of Polyradical Microspheres via Additive-Free Precipitation Photopolymerization and Solid-State Postfunctionalization

As a basis for the polyradical postfunctionalized microspheres, we synthesized the initial nonfunctionalized microspheres along the lines of our previously published synthesis platform.^[9] The solely light-driven precipitation photopolymerization allows for an additive-free synthesis of microspheres at ambient conditions. The precipitation photopolymerization is based on the Diels–Alder cycloaddition of methylisophthalaldehydes (AA) and bis-maleimides (BB) (refer to Figure 1a, and Section S3 in the Supporting Information for the detailed monomer synthesis). Upon light irradiation at 385 nm (centered light-emitting diode (LED) emission), the AA monomer forms successively two highly reactive *ortho*-quinodimethane (*o*-QDM) units, which react as dienophile toward the BB monomer. When the linear photopolymer reaches a critical molecular weight ($M_{n,crit}$), it precipitates spontaneously forming microspheres.^[9] To increase the critical molecular weight, we selected acetone as the reaction solvent and *N,N'*-bismaleimide as highly soluble BB monomer ($c_{AA} \approx c_{BB} = 10 \text{ mmol L}^{-1}$). With this formulation, we achieved a yield of 77% in a batch reactor after isolating the microspheres by centrifugation from the turbid reaction solution. The obtained microspheres are narrow dispersed ($\mathcal{D} = 1.05$) with a number-average diameter (D_n) of 1.48 μm (refer to Section S10 in the Supporting Information).

The optimized *N,N'*-bismaleimide-based formulation furthermore results in the solubility of the photopolymer in dimethyl sulfoxide (DMSO), which allowed us for the first time to characterize the photopolymer by size-exclusion chromatography (SEC) and ¹H-NMR spectroscopy (refer to Figures S14 and S12 in the Supporting Information). The ¹H-NMR spectra allowed us to confirm the formation of the expected polyhexahydro-phenalene-1,6-diol diimide (*p*-HPDD) backbone and the SEC chromatograms revealed a molecular weight M_n

of 25 kDa with a dispersity \mathcal{D} of 4.12 (based on the calibration with narrow dispersed poly(methyl methacrylate) (PMMA) calibration standards). By comparison with the SEC results from the centrifugate containing the soluble low-molecular-weight polymer fraction, we estimate that $M_{n,crit}$ for the nucleation is about 15–20 kDa. However, the molecular weight overlap of the residual polymer from the centrifugate and the isolated microspheres spans over a wide range of 1–65 kDa. We therefore conclude that the microparticles consist of a highly dispersed polymer, even partially below its $M_{n,crit}$.

The postfunctionalization of the initial photopolymerized microspheres toward the polyradical and paramagnetic microspheres is based on our previous work^[17] on small molecules in

solution. Therein, the initial HPDD cycloadduct was converted to tetrahydrophenalen diimides (THPDs) by the E1 elimination of two hydroxy groups and in a second step oxidized to form phenalenyldiimide neutral radicals (PLYDs). Herein, we apply the same chemical transformations to the beforementioned photopolymerized microspheres in the solid state in order to obtain microspheres with a stable neutral delocalized radical in the polymer backbone (refer to Figure 1a). Therefore, we post-treated the *p*-HPDD or “initial” microspheres with *p*-toluenesulfonic acid (*p*-TsOH) for 30 h at 115 °C in toluene to generate the “eliminated” *p*-THPD microspheres and subsequently oxidized them with 2,3-dichloro-5,6-dicyano-1,4-benzochinon (DDQ) in toluene to form “polyradical” *p*-PLYD microspheres. Noteworthy, the microspheres retain their shape and size during this postfunctionalization ($D_{n,polyradical} = 1.46 \mu\text{m}$).

The presence of the stable neutral radical in the polyradical microspheres is substantiated by superconducting quantum interference device (SQUID) measurements and electron paramagnetic resonance (EPR) spectroscopy, evidencing the paramagnetism of the microspheres (refer to Figure 1c and Figure S15 in the Supporting Information). Directly after the elimination, the postfunctionalized microspheres become completely insoluble in any conventional solvent, which complicates following the reaction progression. Following the reaction progression—i.e., assessing the inner chemical distribution of the microspheres—is, however, of utmost interest for the application and optimization of the material system, as the insolubility of the eliminated and the polyradical polymer suggests a diffusion limited penetration of the reactants into the microspheres and an incomplete postfunctionalization. Such a diffusion-limited postfunctionalization would manifest in a core–shell structure with a nonfunctionalized core and a polyradical or mixed eliminated/polyradical shell (refer to Figure 1d). When assessing a possible core–shell structure, the nanometer-sized features and the near-identical chemical structure and composition of the initial, eliminated, and polyradical polymers pose significant challenges. We meet the required high analytical sensitivity and spatial resolution by directly visualizing the inner chemical distribution of the postfunctionalized microspheres based on characteristic electron energy loss signals in the TEM.

2.2. Characteristic Optical Excitations in the TEM Reveal Homogeneous Chemical Distribution

Even though the presence of the stable neutral radicals is evident from the paramagnetism of the microspheres, we herein answer the key question if the elimination and oxidation translate fully through the microspheres and if the postfunctionalization is diffusion-limited to form core–shell-like chemical distribution.

The experimental procedure to reveal the inner chemical distribution of the microspheres is depicted in Figure 2. After embedding the microspheres in an epoxide matrix (EPON), we employed ultramicrotomy to prepare ultrathin electron transparent sections for TEM. The employed TEM is equipped with a monochromator and an electron spectrometer, allowing us to record high-resolution low-loss EEL spectra of

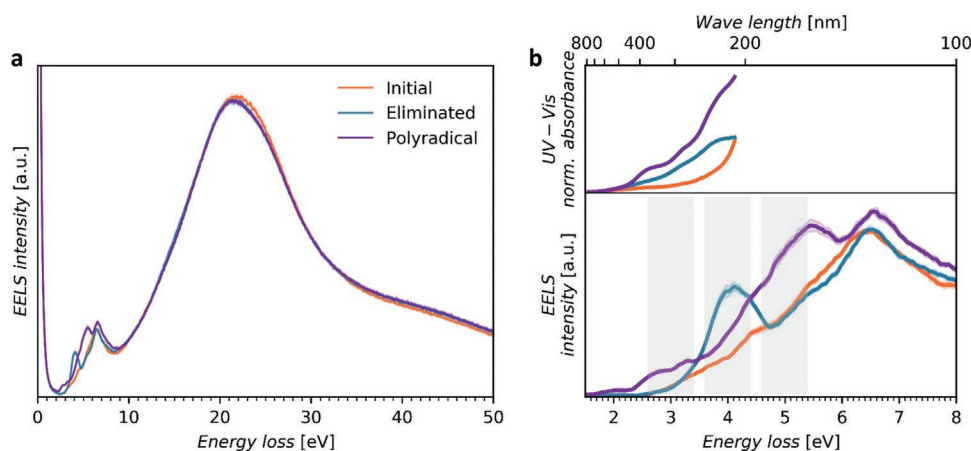


Figure 3. EELS and UV-vis spectroscopy of the microspheres reveal characteristic optical excitations. a) Low-loss EEL spectra. To obtain a quantitative comparison, the spectra are normalized over the integral of the volume plasmon peaks (10–50 eV energy loss). b) UV-vis (top) and EEL spectra (bottom) in the optical range. For this comparison, the zero-loss peaks of the EEL spectra are removed by an exponential fit (cf. Figures S19–S21, Supporting Information). The gray energy regions indicate the energy windows for ESI (cf. Figure 5a) of the specific excitations of the eliminated (4 ± 0.4 eV) and polyradical polymer (3 and 5 ± 0.4 eV). The errors of the EEL spectra were calculated from the standard deviation from the average of ten (initial) or eight (eliminated and polyradical) spectra and are displayed as semi-transparent colored areas around the spectra.

the microspheres (refer to **Figure 3a**). The most intense feature of the low-loss EELS spectra is the volume plasmon peak with around 22 eV energy loss. By utilizing volume plasmon signals, we were previously able to visualize the chemical distribution of organic heterostructures with low-contrast material combinations and track solid-state reactions time-resolved with nanometer resolution.^[18,19] This is, however, not possible for the present polymers, as their volume plasmon signals are almost identical, reflecting their highly similar chemical composition and structure. Only the very low energy loss signals corresponding to optical excitations show characteristic spectral differences, as revealed by EELS and UV-visible spectroscopy (UV-vis, **Figure 3b**). The initial microspheres exhibit overall the lowest EELS and UV-vis signal in the range from 1.5 to 4.1 eV. The polyradical microspheres show in both spectra a consistently stronger spectral signal than the initial none postmodified microspheres. The minor excitations of the polyradical microspheres with an energy loss of 1.7–3.4 eV coincide very well with the respective absorption peaks in UV-vis spectroscopy. The resemblance between UV-vis and EELS is, however, broken by the characteristic EELS excitation of the eliminated microspheres at 4.1 eV, while only intermediate UV-vis absorption occurs. We rationalize the deviations between UV-vis and EELS by the different excitation probabilities for high-energy electrons used in TEM and photons.^[20] The characteristic EELS excitation at 4.1 eV energy loss is unique for the eliminated polymer. The complete absence of this peak in the spectrum of polyradical microspheres indicates a high level of conversion for the oxidation.

Outside the UV-vis range, the initial microspheres show a pronounced excitation at an energy loss of 6.45 eV, which is slightly shifted to 6.5 and 6.55 eV in the eliminated and polyradical microspheres, respectively. We attribute this shift to a denser packing of the polymers after the elimination and oxidation, which may lead to a better electronic coupling in the materials and thus an observed slightly higher excitation energy.

The polyradical microspheres show a pronounced excitation at about 5.5 eV energy loss, which represents, together with the minor excitations from 1.7 to 3.4 eV, the characteristic spectral feature of the polyradical. The small shoulder on this peak at 4.4 eV coincides with a shoulder in the spectrum of the initial microspheres at the same energy loss and overlaps with the pronounced excitation of the eliminated polymer at 4.1 eV. Without additional analysis, which would be well beyond the scope of this study, we cannot conclude whether this shoulder corresponds to a common excitation of all three polymers or indicates incomplete conversion from the initial polymer. However, when comparing the overall peak intensities (refer to **Figure 3a,b**) with the high intensity of the characteristic excitation at 5.5 eV in the polyradical microspheres, it is most likely that this signal derives from one single material, indicating an overall high conversion for the elimination.

In contrast to UV-vis spectroscopy, where the electronic excitations are probed as an ensemble, EELS allows probing the electronic excitations locally, and therefore, allows access to the chemical distribution of the microspheres. Thereby, the characteristic excitations of the eliminated polymer at 4.1 eV and of the polyradical up to 3.4 and at 5.5 eV can serve as spectral fingerprints of the materials and allow their unambiguous identification.

In a first attempt to reveal the chemical distribution of the postmodified microspheres, we acquired EEL spectra (**Figure 3a**) from the center and the edge of the microspheres via a selective aperture, which restricts the acquisition area on the sample to a diameter of 350 nm (**Figure 4a**). To ensure probing the chemical distribution at the center of the microspheres, we only acquired spectra from particle cross sections with a diameter close to or above the average diameter (cf. acquisition area mapping; **Figure S18**, Supporting Information). No spectral differences between the edge and center exist in the initial microspheres. In the eliminated and polyradical microspheres, the intensities of the characteristic excitations at 4.1 and 5.5 eV, respectively, slightly deviate between the edge

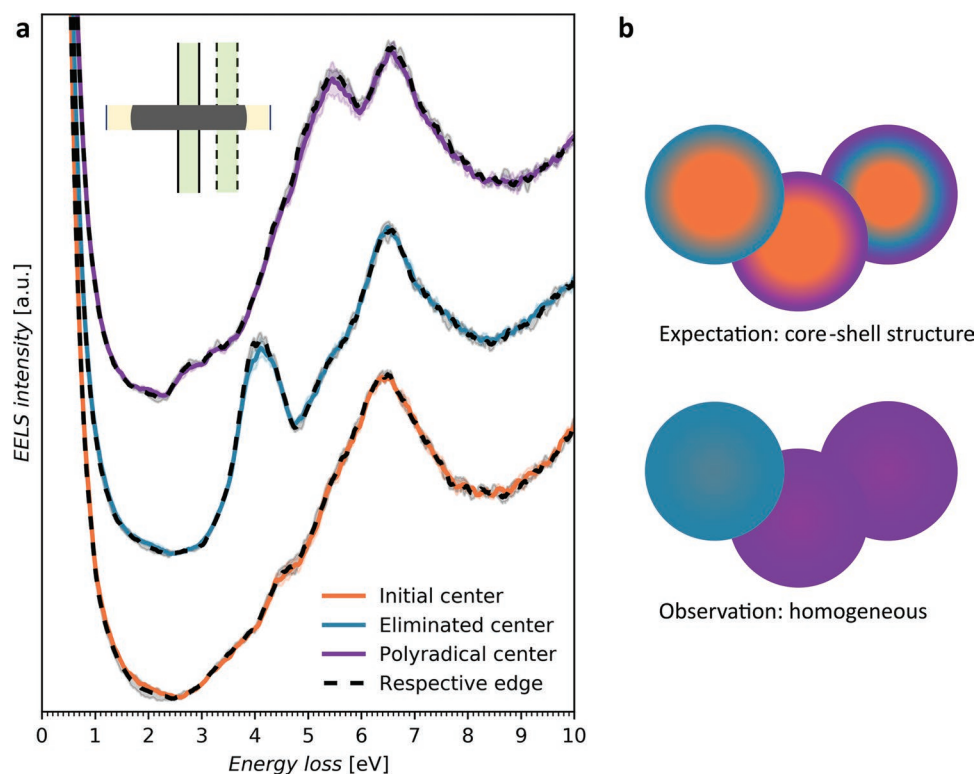


Figure 4. Spatially resolved EELS reveals quasi-homogeneous microspheres. a) EELS at the center (solid lines) and at the edge of the particles (dashed lines). The inset illustrates the position of the selected sample area on the ultrathin section during EELS acquisition. Please refer to Figure S18 (Supporting Information) for the exact positioning of the selected sample area for each spectrum. The errors of the EEL spectra were calculated from the standard deviation from the average of five (initial) or four (eliminated and polyradical) spectra and are displayed as semitransparent colored areas around the spectra. An arbitrary offset was applied to separate the spectra in the plot. b) Illustration of a possible chemical distribution and the observed quasi-homogeneous microspheres.

and the center. However, these minor deviations lie well within the error of the experiment. We therefore conclude that the eliminated and polyradical microspheres are basically homogeneous, opposing the assumption of a core-shell structure (refer to Figure 4b).

We support the finding of homogeneous microspheres by directly imaging their chemical distribution via ESI. For ESI, the spatial resolution is not limited by a selective aperture and the corresponding projected acquisition area. Thus, even an extremely thin potential shell below the resolution limit of the aperture would be resolved. **Figure 5a** shows ESI and standard TEM bright-field images of binary microsphere mixtures of polymerized and eliminated microspheres (Figure 5a, top row), as well as of eliminated and polyradical microspheres (Figure 5a, bottom row). The dark ring at the edge of the bright-field images is caused by the support film of the TEM grid. The microspheres themselves appear as dark ellipses within the brighter embedding EPON matrix. The elliptical shape is a result of the compression during ultramicrotomy. The bright-field intensities of the three polymers appear to differ slightly (refer to Figure 5a first column), as the initial microspheres appear slightly brighter than the eliminated microspheres, which again appear slightly brighter than the polyradical microspheres. This bright-field contrast is most likely a result of the different densities of the initial, eliminated, and polyradical polymers. However, the observed

density contrast barely allows us to distinguish the different microspheres and is far too subtle to identify the chemical distribution within one microsphere. Furthermore, the density contrast is superimposed by thickness variations, e.g., from ultramicrotomy artifacts (refer to Figure S22 in the Supporting Information), underpinning the necessity to utilize ESI to visualize the chemical distribution of the microspheres, as it relies on material-specific electronic excitations and allows us to mitigate thickness influences.

Similar to bright-field imaging, thickness variations influence the ESI intensities and can be falsely interpreted as a variation in chemical distribution.^[21] To minimize these thickness contributions, we normalized the ESI images pixelwise over the integral of the ESI images in the volume plasmon range from 10 to 40 eV energy loss (refer to Figure 3a). Interestingly, we observed an unexpected,^[22] inverse intensity relation between thickness and ESI intensity for the eliminated and polyradical states. We explain this inverse intensity relation by the special ratio between elastically and inelastically scattered electrons at the given experimental conditions.^[23] Please refer to Section S13b (Supporting Information) for more details.

From the EEL spectra we derived the ideal ESI energy windows for imaging the microspheres at 3, 4, and 5 eV energy losses (Figure 3b). These energy windows result in peak ESI intensities for the polyradical microspheres at 3 and 5 eV, and peak ESI intensities for the eliminated microspheres at 4 eV

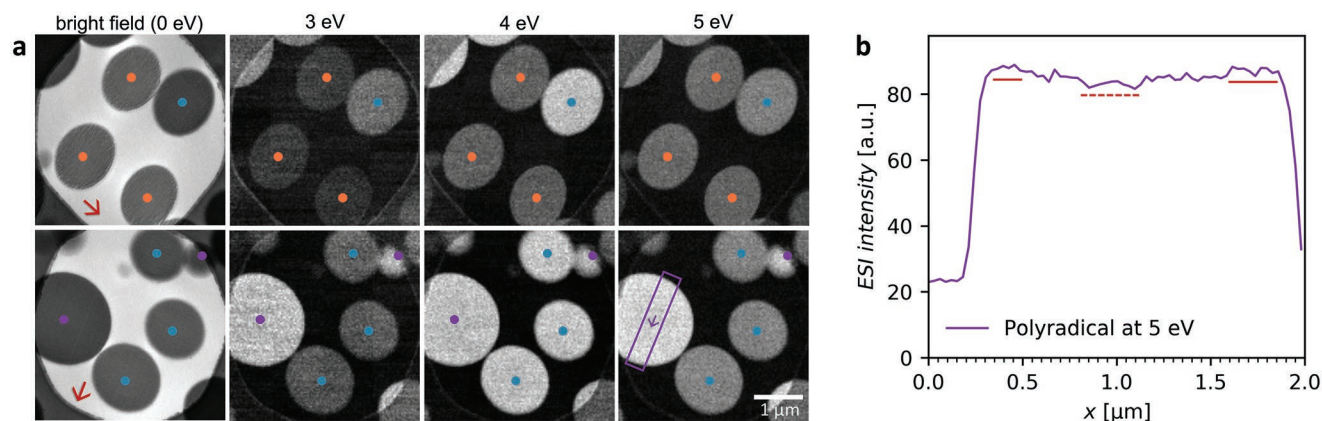


Figure 5. ESI of the characteristic excitations of the three different materials confirms quasi-homogeneous particles. a) Top row: ESI images of a mix of initial (orange dots) and eliminated (blue dots) microspheres. Bottom row: ESI images of a mix of eliminated (blue dots) and radical (purple dots) microspheres. Energy loss values indicate the three windows used for ESI (refer to Figure 3b). Deviations between the experimental ESI intensities from the EEL spectra expected intensities result from the slightly different experimental conditions chosen for both methods (refer to experimental details in Section S13c in the Supporting Information). The red arrows in the bright-field images indicate directions of cutting. Scale applies to all images. The purple frame indicates the line profile in (b). b) ESI intensity profile. The averaged intensity at the edge of the particle (solid red line) and the center of the particle (dashed red line) is 5% at a particle diameter of 1.8 μm .

(refer to Figure 5a). The initial microspheres display the lowest intensity at each of the selected energy windows. The direct imaging of the characteristic optical excitation via ESI confirms the homogeneous chemical distribution of the microspheres. The microspheres in all three states appear as homogeneous ellipses in the ESI images. In fact, a mild, barely perceivable intensity gradient is present in the eliminated and polyradical microspheres (cf. Figure 5b). However, this gradient shows only an intensity difference of maximal 5% between the edge and center of a relatively large microsphere with a diameter of 1.8 μm . Thus, the EELS results are confirmed, the expected core-shell structure is ruled out, and the microspheres can be regarded as homogeneous.

3. Discussion

3.1. Probing Chemical Distributions in the TEM

Herein, we have directly visualized the chemical distribution of photopolymerized and postfunctionalized microspheres with high spatial resolution and chemical sensitivity. The high chemical sensitivity—mandated by the high chemical similarity of the initial polymer and its eliminated and polyradical adducts—was achieved by utilizing the electron energy loss signal of characteristic optical excitations by EELS and ESI in the TEM. We used ultrasonic ultramicrotomy to prepare electron transparent samples for TEM and access the inner chemical distribution of the postfunctionalized microspheres. Ultramicrotomy is a well-established sample preparation technique in biology and medical research, and is recently more and more applied in materials science, especially for the visualization of micro- and nanoscale polymer structures.^[24–26] For soft matter materials, a reactive metal staining (e.g., RuO_4 or OsO_4) is usually applied to generate contrast between the embedding medium and the various materials of interest. However, reactive staining is rather indirect and not suitable to visualize the chemical distribution

accurately in the present edge case and spectroscopic information was needed.

The most common spectroscopic methods in the TEM and scanning TEM (STEM) to visualize chemical distributions are energy-dispersive X-ray spectroscopy (EDS) and core loss EELS. Both methods rely on core ionization of the sample atoms and can, in principle, reach atomic resolution.^[27–30] However, they rely on variations in elemental compositions, which makes them unsuitable for the material system studied here. Furthermore, atomic resolution can only be reached for crystalline, beam stable samples, and the signal-to-noise ratio (SNR) is inferior to low-loss EELS (energy loss <50 eV), especially for the light elements of polymeric materials. Low-loss EELS is dominated by the excitations of the valence electrons, of which the volume plasmon yields the strongest signal. As noted, the volume plasmon signal can be used to visualize the chemical distribution of low-contrast organic heterostructures with nanometer resolution,^[18,21,31,32] which was not possible for the current material system due to near-identical volume plasmon excitations. At similar resolution, 4D STEM revealed the chemical distribution in a blend of comparable systems by utilizing the characteristic pair distribution functions of the mixed semiconductive polymer and fullerene derivative.^[33] However, this seems not feasible for the present system with similar molecular structure of the initial, eliminated, and polyradical polymers. Overall, only the EELS signal of their characteristic optical excitations allowed an unambiguous identification and visualization of the compositionally and structurally similar materials.

EELS and ESI are frequently used to visualize the optical excitations of inorganic plasmonic structures with nanometer resolution.^[34] For the organic materials at hand, the resolution is limited to the upper nanometer range by the unfavorable SNR rather than by the physical limits of the technique, as the characteristic excitations we use in our study vanish with increasing electron exposure. The unfavorable SNR is thus a result of the low signal intensity obtained when avoiding beam

damage. In case higher resolution is required, cryo-TEM can retard beam damage of organic materials by a factor of 3–10 and greatly enhance SNR, and thus, resolution.^[35]

The large EELS intensities of the characteristic optical excitations of the eliminated and polyradical microspheres indicate a high conversion for the elimination and oxidation in the solid state. Yet, we cannot, at this point, conclude whether full conversion has been reached due to the potentially similar or overlapping excitations of the tree states. However, with exact knowledge of the optical excitations of the polymers, e.g., from computational studies, the spectra of the microspheres could, in principle, be deconvoluted and the conversions quantified.

Modern polymeric materials are critically progressing toward complex multifunctionalities and insoluble polymer networks with controllable properties as well as precise nanomorphologies.^[36–38] Thus, standard analytical methods, such as UV–vis, mass spectrometry, NMR, and IR, must be complemented by microscopy methods with spatial resolution in the nanometer range and high chemical sensitivity. Therefore, the role of EELS,^[39] tip-enhanced spectroscopy,^[40,41] and optical super-resolution microscopy^[42] will drastically increase in polymer science, as these methods allow visualization of chemical distributions at the micro- and nanoscale based on optical, IR, or fluorescence signals.

3.2. Photopolymer-Based Stable Neutral Radicals Promise New Applications for Polyradicals

The initial microspheres were synthesized by a Diels–Alder cycloaddition in dispersed media. This light-induced two-component photopolymerization leads to direct precipitation of microspheres without any additives, surfactants, initiators, or heating. Our simple synthesis at mild conditions circumvents typical disadvantages of classic thermal particle synthesis. Furthermore, modification of the backbone or via binding to residual reactive groups at the microsphere surface makes a wide range of functionalizations accessible.^[9] Herein, we expand this range by introducing a stable neutral radical into the polymer backbone to form a paramagnetic polyradical. Polyradicals promise application in data storage,^[43] organic photovoltaics,^[44] batteries,^[45,46] and spintronics.^[47] An application of the system, at hand, for organic batteries seems plausible due to the π -conjugated radical in the backbone and the bandgap of 1.7 eV (determined from the onset of the background subtracted EELS in Figure 3b). Furthermore, the photosynthetic approach as well as the easy synthesis and functionalization of magnetic microspheres promise for polyradicals yet unexplored applications.

Magnetic particles are used for the concentration and removal of compounds,^[48–50] pollutants,^[51] or bacteria and cells^[52,53] in liquid media by magnetic separation. A tailored surface functionalization of the inorganic or polymeric particles allows them to selectively bind the target, while incorporated super-paramagnetic iron oxide nanoparticles enable magnetic separation. The incorporation of the super-paramagnetic iron oxide nanoparticles into the magnetic particles requires, however, complex and highly controlled multistep syntheses. In the polyradical material, at hand, paramagnetism is inherent to the stable neutral radical in the backbone.

Furthermore, the photochemical-based synthesis of the material system offers the potential to utilize the system in light printing and direct laser writing.^[54] Especially, the latter will open interesting applications in micromechanics and even metamaterials with magnetic stimulus.

Despite the analytical challenges imposed by the beam sensitivity and chemical similarity of the initial, eliminated, and polyradical polymers, we were able to evidence homogeneous microspheres and a high conversion to the polyradical. This is especially surprising, as the elimination of the OH-groups creates a highly hydrophobic polymer, which limits the diffusion of the hydrophilic *p*-TsOH into the microspheres even further. Possible, yet to investigate, explanations for these unexpected results are an undiscovered porosity, which is not obvious from the EM images, residual solvent content of the microspheres, and a hopping mechanism of the elimination and oxidation reactions. Finding homogeneous microspheres instead of the expected core–shell structures raises the interesting question of how much our previously demonstrated fluorescent functionalization^[9] affects the volume of the microspheres. Overall, the unexpected result of homogeneous microspheres is a vital proof for the applicability of the material system, as even relatively large micrometer-sized structures can be functionalized efficiently throughout. Furthermore, the combination of ultramicrotomy with EELS and ESI will allow us in the future to optimize the functionalization conditions for differently sized microspheres and structures from direct laser writing.

4. Conclusions

We demonstrate that EELS and ESI can be applied to directly visualize the chemical distribution in polymeric microspheres even for highly similar, beam-sensitive organic materials. Herein, three different polymeric materials derived from a Diels–Alder photopolymerization and a two-step postfunctionalization, i.e., elimination and oxidation, were distinguished by their characteristic optical excitations in the low-energy-loss region of EELS and ESI. To the best of our knowledge, our study constitutes the first example where electron analytical imaging was used to distinguish organic functional materials with almost identical chemical composition and structure. In previous works, similar electron analytical imaging was mainly used for materials of very different chemical composition or structure, e.g., organic solar cells consisting of different material classes such as semiconducting polymers blended with fullerene derivatives or small molecules.

Our analysis of the solid-state postfunctionalization unexpectedly showed chemically homogeneous microstructures for both functionalization reactions, elimination and oxidation. Our findings pose key questions, in particular how the reactants penetrate the solid materials. We anticipate that coupling analytical imaging and low-loss EELS with deeper knowledge about the nature of the optical excitations will allow us to quantify reaction yields by signal deconvolution or the simulation of EEL spectra. Yet, even without quantification, the time-dependent development of the characteristic optical excitations promises unprecedented insights into the underlying mechanism of the unexpected homogeneous functionalization.

Besides these interesting findings regarding the basic chemistry, our material system itself opens key avenues for polymeric microspheres and the manufacturing of functional micro- and nanostructures. Advancing the presented synthetic platform toward precursor materials for other light-based manufacturing schemes, the postfunctionalization grants access to complex microstructures for magnetic metamaterials and micromechanics.

5. Experimental Section

For experimental details, refer to the Supporting Information sections.

Supporting Information

Supporting Information is available from the Wiley Online Library or from the author.

Acknowledgements

The authors acknowledge the help of Dr. Markus Kurth, Gräter group, Heidelberg University, Germany, with the EPR measurements. R.R.S. and C.B.-K. key funding for this project, including the EPR facility, by the Deutsche Forschungsgemeinschaft (DFG, German Research Foundation) under Germany's Excellence Strategy for the Excellence Cluster "3D Matter Made to Order" (EXC-2082/1-390761711), by the Carl Zeiss Foundation and by the Helmholtz program "Materials Systems Engineering." C.B.-K. additionally acknowledges continued support by the Australian Research Council (ARC) in the context of a Laureate Fellowship, enabling his photochemical research program, as well as continued support by QUT's Centre for Materials Science. J.A.K. is currently supported by the Deutsche Forschungsgemeinschaft (DFG, German Research Foundation) with a WBP fellowship—500289223.

Open access publishing facilitated by Queensland University of Technology, as part of the Wiley - Queensland University of Technology agreement via the Council of Australian University Librarians.

Conflict of Interest

The authors declare no conflict of interest.

Author Contributions

J.A.K., F.F. contributed equally to this work. J.A.K. and F.F. shared the experimental part of the study equally, F.F. focused on the synthesis and chemical analysis of the microspheres and J.A.K. performed the ultramicrotomy, electron microscopy imaging, and spectroscopy as well as the data analysis. D.R. supported the study with additional electron microscopy measurements. A.S. supported the study with measurements of the magnetic properties. J.A.K. put together the draft and all authors reviewed and edited the manuscript. All authors were involved in the final interpretation of the results. C.B.-K. and R.R.S. motivated, supervised and funded the work in equal parts.

Data Availability Statement

The data that support the findings of this study are openly available in RADAR4KIT at <https://doi.org/10.35097/884>.

Keywords

chemical distributions, magnetic beads, magnetic polymers, polyradicals, stable neutral radicals

Received: November 27, 2022

Revised: January 5, 2023

Published online: February 26, 2023

- [1] M. C. Brucker, N. J. Macmullen, *J. Obstet. Gynecol. Neonatal. Nurs.* **1985**, *14*, 353.
- [2] M. Feng, J. Chen, J. Xun, R. Dai, W. Zhao, H. Lu, J. Xu, L. Chen, G. Sui, X. Cheng, *ACS Sens.* **2020**, *5*, 2331.
- [3] S. De Koker, B. N. Lambrecht, M. A. Willart, Y. van Kooyk, J. Grooten, C. Vervaeke, J. P. Remon, B. G. De Geest, *Chem. Soc. Rev.* **2011**, *40*, 320.
- [4] O. R. Davies, L. Head, D. Armitage, E. A. Pearson, M. C. Davies, M. Marlow, S. Stolnik, *Langmuir* **2008**, *24*, 7138.
- [5] F. Manger, P. Marlow, K. Fischer, M. Nöller, C. Sprau, A. Colsmann, *Adv. Funct. Mater.* **2022**, *32*, 2202566.
- [6] J. P. Hooker, L. Delafresnaye, L. Barner, C. Barner-Kowollik, *Mater. Horiz.* **2019**, *6*, 356.
- [7] J. P. Hooker, F. Feist, L. Delafresnaye, L. Barner, C. Barner-Kowollik, *Adv. Funct. Mater.* **2020**, *30*, 1905399.
- [8] J. P. Hooker, F. Feist, L. Delafresnaye, F. Cavalli, L. Barner, C. Barner-Kowollik, *Chem. Commun.* **2020**, *56*, 4986.
- [9] L. Delafresnaye, F. Feist, J. P. Hooker, C. Barner-Kowollik, *Nat. Commun.* **2022**, *13*, 5132.
- [10] A. S. Goldmann, L. Barner, M. Kaupp, A. P. Vogt, C. Barner-Kowollik, *Prog. Polym. Sci.* **2012**, *37*, 975.
- [11] D. R. Breed, R. Thibault, F. Xie, Q. Wang, C. J. Hawker, D. J. Pine, *Langmuir* **2009**, *25*, 4370.
- [12] L. Nebhani, D. Schmiedl, L. Barner, C. Barner-Kowollik, *Adv. Funct. Mater.* **2010**, *20*, 2010.
- [13] Q. (Tony) Zhou, L. Qu, T. Gengenbach, J. A. Denman, I. Larson, P. J. Stewart, D. A. V. Morton, *Int. J. Pharm.* **2011**, *413*, 36.
- [14] X. Yang, L.-W. Zhu, L.-S. Wan, J. Zhang, Z.-K. Xu, *J. Mater. Res.* **2013**, *28*, 642.
- [15] K. Mundsinger, C. W. Schmitt, L. Michalek, M. Susewind, T. Hofe, C. Barner-Kowollik, L. Barner, *ACS Macro Lett.* **2020**, *9*, 1785.
- [16] N. T. S. Khomami, A. Welle, S. Kunz, A. Philippe, *Coatings* **2022**, *12*, 335.
- [17] F. Feist, S. L. Walden, J. Alves, S. V. Kunz, A. S. Micallef, A. J. Brock, J. C. McMurtrie, T. Weil, J. P. Blinco, C. Barner-Kowollik, *Angew. Chem., Int. Ed.* **2021**, *60*, 10402.
- [18] W. Köntges, P. Perkhun, J. Kammerer, R. Alkarsifi, U. Würfel, O. Margeat, C. Videlot-Ackermann, J.-J. Simon, R. R. Schröder, J. Ackermann, M. Pfannmöller, *Energy Environ. Sci.* **2020**, *13*, 1259.
- [19] J. A. Kammerer, X. Duan, F. Neubrech, R. R. Schröder, N. Liu, M. Pfannmöller, *Adv. Mater.* **2021**, *33*, 2008259.
- [20] D. B. Lingerfelt, P. Ganesh, J. Jakowski, B. G. Sumpter, *J. Chem. Theory Comput.* **2020**, *16*, 1200.
- [21] M. Pfannmöller, H. Flügge, G. Benner, I. Wacker, C. Sommer, M. Hanselmann, S. Schmale, H. Schmidt, F. A. Hamprecht, T. Rabe, W. Kowalsky, R. R. Schröder, *Nano Lett.* **2011**, *11*, 3099.
- [22] R. F. Egerton, *Phys. Status Solidi A* **1976**, *37*, 663.
- [23] I. Angert, C. Burmester, C. Dinges, H. Rose, R. R. Schröder, *Ultramicroscopy* **1996**, *63*, 181.
- [24] T. R. Guimaraes, M. Khan, R. P. Kuchel, I. C. Morrow, H. Minami, G. Moad, S. Perrier, P. B. Zetterlund, *Macromolecules* **2019**, *52*, 2965.
- [25] F. Mayer, D. Ryklin, I. Wacker, R. Curticean, M. Čalkovský, A. Niemeyer, Z. Dong, P. A. Levkin, D. Gerthsen, R. R. Schröder, M. Wegener, *Adv. Mater.* **2020**, *32*, 2002044.

- [26] V. Hahn, T. Messer, N. M. Bojanowski, E. R. Curticean, I. Wacker, R. R. Schröder, E. Blasco, M. Wegener, *Nat. Photonics* **2021**, *15*, 932.
- [27] K. Kimoto, T. Asaka, T. Nagai, M. Saito, Y. Matsui, K. Ishizuka, *Nature* **2007**, *450*, 702.
- [28] M. Bosman, V. J. Keast, J. L. García-Muñoz, A. J. D'Alfonso, S. D. Findlay, L. J. Allen, *Phys. Rev. Lett.* **2007**, *99*, 086102.
- [29] A. J. D'Alfonso, B. Freitag, D. Klenov, L. J. Allen, *Phys. Rev. B* **2010**, *81*, 100101.
- [30] M.-W. Chu, S. C. Liou, C.-P. Chang, F.-S. Choa, C. H. Chen, *Phys. Rev. Lett.* **2010**, *104*, 196101.
- [31] L. F. Drummy, R. J. Davis, D. L. Moore, M. Durstock, R. A. Vaia, J. W. P. Hsu, *Chem. Mater.* **2011**, *23*, 907.
- [32] R. F. Egerton, *Ultramicroscopy* **2007**, *107*, 575.
- [33] X. Mu, A. Mazilkin, C. Sprau, A. Colsmann, C. Kübel, *Microscopy* **2019**, *68*, 301.
- [34] F. J. García de Abajo, *Rev. Mod. Phys.* **2010**, *82*, 209.
- [35] R. F. Egerton, *Micron* **2019**, *119*, 72.
- [36] A. S. Abd-El-Aziz, M. Antonietti, C. Barner-Kowollik, W. H. Binder, A. Böker, C. Boyer, M. R. Buchmeiser, S. Z. D. Cheng, F. D'Agosto, G. Floudas, H. Frey, G. Galli, J. Genzer, L. Hartmann, R. Hoogenboom, T. Ishizone, D. L. Kaplan, M. Leclerc, A. Lendlein, B. Liu, T. E. Long, S. Ludwigs, J. Lutz, K. Matyjaszewski, M. A. R. Meier, K. Müllen, M. Müllner, B. Rieger, T. P. Russell, D. A. Savin, et al., *Macromol. Chem. Phys.* **2020**, *221*, 2000216.
- [37] S. P. O. Danielsen, H. K. Beech, S. Wang, B. M. El-Zaatari, X. Wang, L. Sapir, T. Ouchi, Z. Wang, P. N. Johnson, Y. Hu, D. J. Lundberg, G. Stoychev, S. L. Craig, J. A. Johnson, J. A. Kalow, B. D. Olsen, M. Rubinstein, *Chem. Rev.* **2021**, *121*, 5042.
- [38] V. X. Truong, K. Ehrmann, M. Seifermann, P. A. Levkin, C. Barner-Kowollik, *Chem. – Eur. J.* **2022**, *28*, e202104466.
- [39] J. A. Hachtel, J. Huang, I. Popovs, S. Jansone-Popova, J. K. Keum, J. Jakowski, T. C. Lovejoy, N. Dellby, O. L. Krivanek, J. C. Idrobo, *Science* **2019**, *363*, 525.
- [40] V. J. Rao, M. Matthiesen, K. P. Goetz, C. Huck, C. Yim, R. Siris, J. Han, S. Hahn, U. H. F. Bunz, A. Dreuw, G. S. Duesberg, A. Pucci, J. Zaumseil, *J. Phys. Chem. C* **2020**, *124*, 5331.
- [41] A. Jarzembki, C. Shaskey, K. Park, *Front. Energy* **2018**, *12*, 43.
- [42] D. V. Chapman, H. Du, W. Y. Lee, U. B. Wiesner, *Prog. Polym. Sci.* **2020**, *111*, 101312.
- [43] P. Hewitt, D. A. Shultz, *Appl. Magn. Reson.* **2020**, *51*, 1331.
- [44] X. Lv, J. Mao, Y. Liu, Y. Huang, Y. Ma, A. Yu, S. Yin, Y. Chen, *Macromolecules* **2008**, *41*, 501.
- [45] K. Oyaizu, H. Nishide, *Adv. Mater.* **2009**, *21*, 2339.
- [46] F. Li, Y. Zhang, S. R. Kwon, J. L. Lutkenhaus, *ACS Macro Lett.* **2016**, *5*, 337.
- [47] K. Tagami, M. Tsukada, *J. Phys. Chem. B* **2004**, *108*, 6441.
- [48] Z. Zou, M. Ibisate, Y. Zhou, R. Aebbersold, Y. Xia, H. Zhang, *Anal. Chem.* **2008**, *80*, 1228.
- [49] Q. Liu, J. Shi, M. Cheng, G. Li, D. Cao, G. Jiang, *Chem. Commun.* **2012**, *48*, 1874.
- [50] M. Shao, F. Ning, J. Zhao, M. Wei, D. G. Evans, X. Duan, *J. Am. Chem. Soc.* **2012**, *134*, 1071.
- [51] C. Liang, R. Ristic, V. Jiranek, D. W. Jeffery, *J. Agric. Food Chem.* **2018**, *66*, 7121.
- [52] K. El-Boubbou, C. Gruden, X. Huang, *J. Am. Chem. Soc.* **2007**, *129*, 13392.
- [53] W. Zhao, T. Zhu, R. Cheng, Y. Liu, J. He, H. Qiu, L. Wang, T. Nagy, T. D. Querec, E. R. Unger, L. Mao, *Adv. Funct. Mater.* **2016**, *26*, 3990.
- [54] M. Gernhardt, V. X. Truong, C. Barner-Kowollik, *Adv. Mater.* **2022**, *34*, 2203474.